

# Journal of Offshore Mechanics and Arctic Engineering

Issues Accepted Manuscripts All Years Purchase For Authors ▾ About ▾



## RESEARCH-ARTICLE

### Numerical and Experimental Analysis of Added Resistance of Ships in Waves


Ould el Mactar, Sebastian Sigmund, Jens Ley, Thomas E. Schellin



+ Author and Article Information

*J. Offshore Mech. Arct. Eng.* Feb 2017, 139(1): 011301 (9 pages)

**Paper No:** OMAE-15-1051 <https://doi.org/10.1115/1.4034205>

**Published Online:** September 30, 2016 [Article history](#) 

 Standard View  PDF  Share ▾  Cite

 Permissions



Contents



Data & Figures



References



Related

Two Reynolds-Averaged Navier–Stokes (RANS) based field methods numerically predicted added resistance in regular head waves for a 14,000 TEU containership and a medium size cruise ship. Long and short waves of different frequencies were considered. Added resistance was decomposed into diffraction and radiation force components, whereby diffraction forces were obtained by restraining the ship in waves and radiation forces by prescribing the motions of the ship in calm water. In short waves, the diffraction part of total resistance was dominant as almost no ship motions were induced. In long waves, the sum of diffraction and radiation forces exceeded total resistance, i.e., the interaction of these two force components, which caused the reduction of total resistance, needed to be accounted for. Predictions were compared with model test measurements. Particular emphasis was placed on the following aspects: discretization errors, frictional resistance as part of total added resistance in waves, and diffraction and radiation components of added resistance in waves. Investigations comprised two steps, namely, a preliminary simulation to determine calm water resistance and a second simulation to compute total resistance in waves, always using the same grids. Added resistance was obtained by

subtracting calm water resistance from total averaged wave resistance. When frictional resistance dominated over calm water resistance, which holds for nearly all conventional ships at moderate Froude numbers, high grid densities were required in the neighborhood surrounding the hull as well as prism cells on top of the model's surface.

**Issue Section:** [Offshore Technology](#)

**Keywords:** [Hydrodynamics](#), [Ship motions](#), [Risers](#), [Cable dynamics](#), [Moorings](#)

**Topics:** [Ships](#), [Waves](#), [Simulation](#)

## Introduction

Prediction of added resistance of ships in waves is of high practical interest. Naturally, therefore, a considerable amount of research effort has been devoted to this problem. Techniques used to predict added resistance can be classified into two main categories, namely, far-field methods, based on considering diffracted and radiated wave energy and momentum flux at infinity, and near-field methods, based on direct integration of steady second-order hydrodynamic pressures acting on the wetted ship surface. Maruo [1] introduced the first far-field approach, which he later extended. Boese [2] developed the first near-field direct pressure integration method, albeit by considering a highly simplified pressure distribution. Gerritsma and Beukelman [3] introduced the radiated energy approach, which basically followed Maruo's far-field approach. Evaluating the above approaches, Strom-Tejsen et al. [4] found large discrepancies between numerical results and comparative model test measurements. Using ship motions obtained from strip theory, Salvesen et al. [5] obtained satisfactory predictions by applying Gerritsma and Benkelman's method, thereby confirming the importance of accurate ship motion predictions to reliably estimate added resistance. By introducing a simplified added resistance formula to model the complicated interaction of diffracted waves and the steady flow around the ship, Faltinsen et al. [6] presented a more accurate potential theory near-field direct pressure integration approach. In this way, they validated their results even for short waves. Recently, Liu et al. [7] used a well-established frequency domain panel method and a new hybrid time domain Rankine source Green function method to predict added resistance in waves by obtaining the first-order velocity potentials and Kochin functions, terms necessary to compute added resistance according to Maruo's far-field method. They used a wide range of

case studies to validate their results and concluded that their method is satisfactory to predict added resistance of ships in waves.

The three-dimensional Rankine panel method of Söding et al. [8] accounts for the interaction of the linear periodic wave-induced flow with the nonlinear steady flow caused by the ship's forward speed in calm water, taking into account nonlinear free surface conditions and dynamic squat. Added resistance in waves is obtained by pressure integration. Kashiwagi et al. [9] also investigated the prediction accuracy of added resistance in short waves when forward speed is present and attributed the associated inaccuracies to hydrodynamic nonlinear effects.

While boundary element methods based on Rankine sources are efficient and, therefore, predominantly used to screen relevant wave scenarios for design issues, computational fluid dynamics (CFD) methods based on the numerical solution of RANS or Euler equations are increasingly applied to validate results because they account for such nonlinearities. El Moctar et al. [10] and Schellin and el Moctar [11] demonstrated that these methods are able to provide results of comparable or superior accuracy to model test measurements in many problems of ship hydrodynamics. However, their applications to added resistance predictions are still rare. Although such methods might, in principle, directly address also the problem of power increase in irregular waves (if combined with an engine model), both long waves (and the corresponding large ship motions) and short waves (which contribute to added resistance through diffraction) have to be resolved simultaneously, which significantly increases the required grid size and computation time. Therefore, application of CFD methods to the added resistance problem has been limited so far to regular wave situations in a restricted range of wave frequencies.

We used RANS based field methods to systematically investigate added resistance in regular head waves for a Post-Panamax 14,000 TEU containership referred to as the Duisburg test case (DTC) [12] and a medium-size cruise ship. Predictions of added resistance in waves were compared with each other and with model test measurements. Particular emphasis was placed on discretization errors, frictional and pressure resistance as parts of total added resistance in waves, and radiation and diffraction components of added resistance in waves.

Although added resistance is not generally largest in

head waves, but in slightly oblique 10–20 deg off-bow waves, considering only head waves simplified computations considerably and was, therefore, a pragmatic engineering approach to obtain reasonable estimates [13].

Our investigations comprised two steps, namely, a preliminary simulation to determine calm water resistance and a second simulation to compute total resistance in waves, always using the same grids for both simulations. Added resistance was obtained by subtracting calm water resistance from total averaged wave resistance. As long as frictional resistance dominates over calm water resistance, which holds for nearly all conventional ships at moderate Froude numbers, high grid densities were required in the neighborhood surrounding the hull. The resulting quadratic transfer functions of added resistance in regular waves were computed at model scale to avoid scaling effects. Model tests were performed at Marintek for the DTC and at Hamburgische Schiffbau-Versuchsanstalt (HSVA) and Schiffbau-Versuchsanstalt Potsdam (SVA) for the cruise ship. Both test setups considered six degrees-of-freedom ship motions while using springs to hold the models in position.

## Numerical Methods

The RANS solver COMET [14] and a modified interDyMFoam solver from the CFD utility OpenFOAM [15] were used for numerical simulations. These two solvers implement the interface capturing technique of the volume-of-fluid (VOF) type, which proved to be suitable for handling strong nonlinearities. The solution domain is subdivided into finite volumes for which the conservation equations are solved. For an incompressible, isothermal, and viscous fluid with density  $\rho$ , the governing equations for conservation of mass,  $m = \int_V \rho \, dV$ , and momentum,  $m \cdot \mathbf{v}$ , are

$$\frac{\partial}{\partial t} \int_V \rho \, dV + \int_S \rho (\mathbf{v} - \mathbf{v}_S) \cdot \mathbf{n} dS = 0 \quad (1)$$

$$\frac{\partial}{\partial t} \int_V \rho \mathbf{v} dV + \int_S \rho \mathbf{v} (\mathbf{v} - \mathbf{v}_S) \cdot \mathbf{n} dS = \int_S \mathbf{T} \cdot \mathbf{n} dS \quad (2)$$

In the momentum Eq. (2), the surface and volume forces are included in the stress tensor,  $\mathbf{T}$ , and in the body force,  $\mathbf{b}$ , respectively, where  $V$  is the control volume,  $\mathbf{v}$  is the fluid velocity, and  $\mathbf{v}_S$  is the velocity of the fluid surface,  $S$ . The stress tensor,  $\mathbf{T}$ , includes viscous shear stresses and a pressure term,  $p$ , multiplied by the unit tensor,  $\mathbf{I}$

$$\mathbf{T} = \mu \{ \nabla \mathbf{v} + \nabla \mathbf{v}^T \} - p \mathbf{I} \quad (3)$$

where  $\mu$  is the dynamic viscosity. The second-order scheme ITTL of COMET and the Crank-Nicholson method of OpenFOAM discretize and solve time derivatives, using, respectively, constant time steps and adaptive time steps.

To obtain a dedicated pressure equation, the mass equation is converted into a pressure correction equation. The SIMPLE algorithm of COMET [16] provides an implicit coupling between pressure and velocity. At each time step, outer iterations iteratively correct pressures and velocities. The solver used in OpenFOAM employs the merged PISO-SIMPLE algorithm.

To simulate a body floating in waves, a two phase fluid flow is defined for water and air. In contrast to the level set method, the VOF method satisfies mass conservation. It computes an additional transport equation to obtain the scalar volume fraction,  $\alpha$ , between zero and one to indicate the spatial distribution of each fluid inside each cell. It may be used to describe, for instance, the effective fluid density of cell,  $\rho_{\text{eff}}$ :

$$\rho_{\text{eff}} = \alpha \rho_{\text{water}} + (1 - \alpha) \rho_{\text{air}} \quad (4)$$

where  $\rho_{\text{water}}$  and  $\rho_{\text{air}}$  are densities of water and air, respectively. Code COMET employs the HRIC scheme to discretize the transport equation for  $\alpha$ ; solver OpenFOAM, the explicit MULES algorithm.

At inlet boundaries, a wave boundary condition describes velocities and surface elevation. A linear superposition of wave harmonics according to Airy and the second-order Stokes waves yield the surface elevation. In the fluid field, the orbital velocities are initialized. Rigid body six degrees-of-freedom motion equations are implicitly coupled with the RANS equations to compute ship motions [10]. Related to these ship motions, a mesh morphing method deforms the numerical grid to follow ship motions in the computational domain. Code COMET implements the  $k$ - $\epsilon$  turbulence model; solver OpenFOAM, the  $k$ - $\omega$ -SST turbulence model.

## Resistance and Ship Motions

Added resistance in waves was obtained by subtracting the calm water resistance,  $R_{\text{calm}}$ , from the averaged oscillating total resistance,  $R_T$ . This calm water resistance was obtained by averaging the model's resistance of the respective simulations; total resistance in waves as well as ship motion amplitudes,

by Fourier analyzing at least the last four simulated encounter periods. In simulations and experiments, the nearly undisturbed wave heights were measured amidships far away from ship induced waves. Values of resistance and ship motions are normalized as follows:

$$\widetilde{R}_{aw} = \frac{(R_T - R_{calm}) \cdot L}{\rho g B^2 \zeta_a^2} \quad (5)$$

$$\widetilde{\theta} = \frac{v_a \cdot L}{2\pi \zeta_a} \quad (6)$$

$$\widetilde{z} = \frac{z_a}{\zeta_a} \quad (7)$$

where  $g$  is the acceleration of gravity,  $B$  is the ship breadth,  $L$  is the ship length between perpendiculars,  $\zeta_a$  is the wave amplitude,  $z_a$  and  $\theta_a$  are, respectively, the heave and pitch amplitude, and  $R_{aw}$  is the average value of added resistance in waves. Symbol  $\sim$  identifies normalized values.

As model tests are not suited to predict the frictional resistance component for ships, it is common practice to rely on the ITTC 1957 guidelines (ITTC) to specify a ship's frictional resistance via the nondimensional coefficient,  $C_F$ , written as follows:

$$C_F = \frac{0.075}{(\log Re - 2)^2} \quad (8)$$

where  $Re$  is the Reynolds number,  $Re = v_s L_{pp} / \nu_w$ , with  $v_s$  denoting the ship speed and  $\nu_w$  the kinematic viscosity of water. Frictional resistance,  $R_F$ , was obtained as follows:

$$R_F = 0.5 \rho v_s^2 S_F C_F \quad (9)$$

where  $S_F$  is the wetted surface of the hull.

In an irregular seaway, added resistance is the time mean value of the second-order wave force. This second-order force can be expressed by superimposing regular wave responses, and the average added resistance,  $\overline{R}_{AW}$ , is then

$$R_{aw} = 2 \int_0^\infty R(\omega) S_\zeta(\omega) d\omega \quad (10)$$

where  $R(\omega)$  is the mean added resistance (response) function in regular waves of circular frequency  $\omega$ , and  $S_\zeta(\omega)$  is the spectral density function of the irregular seaway. Therefore, almost all available methods to calculate added resistance in waves focus on regular waves.

The added resistance in regular waves, varying linearly with wave height squared, was thus considered to be a second-order force and presented as a quadratic transfer function

$$R(\omega) = R_{aw}/\zeta_a^2 \quad (11)$$



where  $\zeta_a$  is the wave amplitude.

## Grid Generation and Boundary Conditions

Simulations were performed on unstructured grids consisting of hexahedrons. Dimensions of the computational domain depended on ship model lengths. The inlet boundary was located between one and two model lengths ahead of the model's forward perpendicular; the outlet boundary, three model lengths behind the model's aft perpendicular; the side boundaries, two-and-a-half model lengths to port of the model's central symmetry plane; the bottom, between two and three model lengths below the calm water surface; and the top, between one-half and one-and-a-half model lengths above the calm water surface. To resolve the wave pattern and the incident wave field, grids were locally refined in the vicinity of the free surface and around the hull. Figure 1 shows grid resolution of the computational fluid domain for wave computations in the vicinity of the free surface.

To dampen incident and hull-induced waves, control volumes were smoothly stretched toward the outlet boundaries. To resolve the boundary layer at the hull, prism layers were included and additional logarithmic wall functions applied.

At the inlet boundary, velocities, volume fractions, turbulent kinetic energies, and dissipation rates were specified. Hull surfaces were defined as no-slip walls. At the outlet and top boundaries, the hydrostatic boundary condition was defined, while at the symmetry plane, a symmetry boundary condition was imposed. The origin of the inertial frames was located on the ships' base line at their aft perpendicular. The origin of the ship-fixed reference frames was situated at their center of gravity (CoG). To avoid scaling effects, all simulations were performed at model scale.

Comparative measurements were obtained from scale model tests. For the DTC, these tests were conducted at SVA Potsdam for calm water and at Marintek for waves; for the cruise ship, at HSVA.

Table 1 lists main particulars of the two ship models

investigated.

## The Duisburg Test Case

### Calm Water Resistance.

The ITTC (2011) recommendations served as a guide to select the computational domain surrounding the ship. A ship's symmetry about its center plane allowed discretizing only one-half of this domain. On top of the hull, three prismatic layers were located with dimensionless wall distance,  $y^+$ , ranging between 30 and 300.

Figure 2 shows the global grid configuration for calm water simulations. All gradient, Laplace, and divergence terms were discretized using Gauss integration and linear central difference interpolations.

To investigate the influence of mesh fineness on predictions, simulations using the OpenFOAM RANS solver *interDym-FOAM* were performed on four grids of differing fineness based on changing the base cell size for the ship at  $F_n = 0.218$ . Utilities *blockMesh* and *snappyHexMesh* generated the numerical grids. A simulation on the finest grid with three times as many cells as the coarsest grid took eight times longer than a simulation on the coarsest grid. On finer grids, the increased size of the system of simultaneous equations that had to be solved, and the greater number of associated iterations caused disproportionately longer computation times. Table 2 lists the number of cells, the dimensionless wall distances, and the computation times for simulations on these grids.

The RANS computations integrated shear stresses and pressures separately to provide the frictional contribution,  $R_f$ , the pressure contribution,  $R_p$ , and the total resistance,  $R_T$ . The pressure contribution,  $R_p$ , comprises a wave-making component,  $R_w$ , and a viscous pressure resistance component,  $R_{vp}$ .

For the DTC, Fig. 3 compares RANS computed total resistance,  $R_T$ , the pressure-induced part of total resistance,  $R_p$ , and the frictional resistance,  $R_f$ , obtained on different grids. Results are presented as nondimensional coefficients of total resistance,  $C_T = R_T / 0.5 \rho g v^2 S_w$ , frictional resistance,  $C_F = R_f / 0.5 \rho g v^2 S_w$ , and pressure resistance,  $C_p = C_T - C_F$ . These plots show that as the number of cells increases, i.e., with finer meshes, predictions slowly converge monotonically toward measured values. Frictional resistance is compared with the ITTC'57 friction line.

Figure 3 indicates that component  $R_f$  varies no more



than 1.5% on the four grids, i.e., this component was considered to be independent of grid fineness. Generally, numerical diffusion caused  $R_{VD}$  to be overestimated although, on finer grids, this overestimation diminishes. However, component  $R_W$  increases on finer grids, caused by more accurate resolution of the radiated waves. With greater grid fineness, pressure component  $R_{VD}$  as well as total resistance  $R_T$  first declines at a greater rate than wave component  $R_W$  which increases after reaching a certain degree of grid fineness.

Simulations performed on the medium grid for the fixed DTC advancing at six Froude numbers that ranged from 0.174 to 0.218 and corresponded to full-scale ship speeds between 20 and 25 kts yielded calm water resistances plotted in Fig. 4 together with comparable model test measurements. Numerical simulations underestimate the measured resistances by between 2.15 and 4.12%, with deviations increasing at higher Froude numbers. These deviations are less than 5%, a relatively small amount considering that dynamic forward speed effects on heave and trim were neglected. These simulations demonstrated that reasonably accurate calm water resistances were obtained on a relatively coarse mesh.

### **Resistance in Regular Waves.**

Simulations were performed for DTC advancing at  $F_n = 0.28$  in regular head waves of ten different wavelengths with  $\lambda/L$  ratios ranging between 0.5 and 2.0. Wave height of 0.12 m was the same for all simulations; but ratio  $H/\lambda$ , wave frequency  $\omega$ , and wave encounter frequency  $\omega_e$  changed with different wavelengths as listed in Table 3.

Numerical grid configuration significantly influenced not only the transport of waves, but also the robustness of the simulation deforming the numerical grids. Waves propagating in the negative  $x$ -direction and orbital wave particle motion occurring on the vertical  $x/z$ -plane required refinement of cells in the  $x$ - and  $z$ -directions. In the  $x$ -direction, cells between the inlet boundary and the ship's aft perpendicular and, in the  $z$ -direction, cells underneath the free surface were, therefore, refined. The grids used consisted of about  $800 \times 10^3$  control volumes.

To avoid reflection at the outlet boundary and the sides, cells grew larger in the  $y$ -direction and in the  $x$ -direction behind the model. Refinement of cells on hull sides and bottom and arrangement of prismatic cells on top of the hull were kept the same as those for calm water simulations. The  $y^+$ -values are shown

in Fig. 5 for a simulation in waves of  $\lambda/L = 1.25$ .

On this grid, depending on wave frequency, between 30 and 100 cells discretized each wavelength horizontally, and about 8–10 cells discretized each wave height (referred to the undisturbed wave amidships) vertically.

Waves were initialized in the entire fluid domain. At the inlet boundary, dynamic boundary conditions for wave particle velocities and volume fractions of an incident Airy wave were specified. Simulations lasted for 20 s real-time. Over the first 5.0 s, ship motions were suppressed to avoid results from diverging. Over the next 15 s, the ship was free to heave and pitch. Sample wave patterns from simulations of the ship in head waves of  $\lambda/L = 1.25$  are shown in Fig. 6. Intact regular waves ahead and diffused waves behind the ship can be observed. Figure 7 shows computed and measured response amplitude operators (RAOs) of the added resistance.

To demonstrate the influence of diffraction, Fig. 8 plots resistance in waves for the fixed ship and for the ship free to heave and pitch. For the fixed DTC, resistance remains almost constant for all investigated wavelengths, a consequential situation as resistance was then solely caused by diffraction. For the ship free to heave and pitch, resistance is significantly higher over all of the investigated wavelengths, except in the longest waves. In wavelengths of  $\lambda/L$  ratios around 1.0, resistance for the ship free to heave and pitch is about an order of magnitude higher than for the fixed ship, i.e., the diffraction part of total resistance in these wavelengths is only about one-fifth of total resistance. These results were significant because large and medium sized ships are predominantly exposed to relatively shorter waves of  $\lambda/L$  ratios between 0.2 and 0.8.

For the DTC free to heave and pitch, Fig. 9 shows representative time histories of the numerically simulated longitudinal force acting on the DTC advancing at  $F_n = 0.28$  in regular head waves of three different lengths. The longitudinal forces oscillate periodically at the associated wave frequency. In short waves of  $\lambda/L = 0.44$  as well as in long waves of  $\lambda/L = 2.5$ , the added resistance in waves is relatively small compared to the mean resistance. However, in waves of  $\lambda/L = 1.0$ , the added resistance in waves contributes significantly to the total resistance. The resulting total force oscillations include a second harmonic force component.

# The Cruise Ship

## Calm Water Resistance.

Using code COMET, numerical simulations were performed to obtain calm water resistance for the cruise ship at two speeds corresponding to  $F_n$  of 0.16 and 0.23. Three grids were generated, consisting of about  $750 \times 10^3$  cells for the coarse grid,  $1050 \times 10^3$  cells for the medium grid, and  $1450 \times 10^3$  cells for the fine grid. Grid size was varied using a refinement factor  $r = x_1/x_2 = (1.5)^{1/2}$ , where  $x_1$  and  $x_2$  are base factors for the coarse background grid and the refined grid, respectively. Wall functions were applied and, therefore, the  $y^+$ -value was kept between 50 and 70 [16]. Figure 10 presents the medium grid structure surrounding the cruise ship.

The ship was free to heave and pitch, whereas surge motion was suppressed. Figure 11 shows the resulting time histories of calm water resistance,  $R_T$ , obtained on the three grids together with frictional resistance,  $R_F$ , obtained on the medium grid and frictional resistance according to ITTC recommendations, as well as the corresponding resistance obtained from model test measurements. Experimental results were obtained from tests of the model with appendages; numerical results, from simulations without appendages.

The three time histories from numerical simulations on different grids achieve monotonic convergence, and the frictional component of resistance correlates favorably with ITTC recommendations (deviation of about 1%). Frictional resistance from simulations is almost independent of grid size, a situation consistent with nearly unchanged  $y^+$  values of the first cell, total prism layer thicknesses, and number of prism layers. Thus, total resistance depended solely on the pressure resistance component, which component decreases on finer grids.

Total resistance from model tests exceeds total resistance from numerical simulations on the medium grid by about 7.5% and on the fine grid by about 9.4%. This unexpected behavior occurred because the test model was equipped with a propeller shaft, a rudder, and two bilge keels (appendages), whereas the numerical simulations were conducted with the bare hull. Nevertheless, numerically simulated results were thought to be representative, because neglecting the effects of appendages did not significantly influence added resistance in waves.

## Resistance in Regular Waves.

Simulations were performed for the cruise ship in

regular head waves. To ensure linear and comparable wave profiles, the wave steepness was kept constant at  $H/\lambda = 1/40$  for the entire frequency range of waves with  $\lambda/L$  ratios ranging between 0.21 and 2.2. With the ship free to heave and pitch and surge suppressed, the resulting RAOs of ship motions at  $F_n = 0.23$  generally correlated favorably with comparable experimental measurements [12]. While surge motions of the cruise ship were free in the model tests, the numerical simulations were conducted with restrained horizontal (surge) motions. However, the experimentally measured mean ship speed was forced by the carriage and may be regarded as constant with small fluctuations caused by the inherent vibrations of the carriage. Although relative wave elevations were not evaluated, a check of the relative phase relationships revealed that ship motions were plausible.

At  $F_n = 0.23$ , simulations were performed in regular head waves on the previously introduced coarse, medium, and fine grids, revealing that heave and pitch motions were not significantly influenced by grid density. As seen in Fig. 12, motion responses are nearly identical over the entire frequency range investigated. Nevertheless, grid size does affect resistance in short waves, as shown by the comparative RAOs of resistance on the coarse grid and the medium grid in Fig. 13, due to different actual wave heights. In short waves, ship motions are relatively small and, thus, diffraction predominated. Furthermore, bow waves tended to break in shorter waves, see Fig. 14.

Accordingly, this affected total resistance was plotted in Fig. 15 as quadratic RAOs of resistance coefficients against nondimensional wave frequency. This figure comprises plots of measured resistance coefficients obtained from model tests as well as computed resistance coefficients. Frictional, pressure, and total resistance coefficients were obtained from numerical simulations on the coarse grid and on the medium grid using code COMET. Total resistance coefficients were obtained from numerical simulations only on the coarse grid using code OpenFOAM.

Numerical results using COMET and OpenFOAM were obtained over the same range of frequencies. Numerical results obtained on the coarse grid agree more closely with measurements than numerical results obtained partly on the medium grid. Agreement of total resistance coefficients with measurements is least favorable in wave frequencies of  $\lambda/L$  ratios near unity. In this frequency range, RAOs

of ship motions differ most from model test measurements [12].

The frictional resistance component is hardly affected by grid discretization. Therefore, deviations from measurements of total resistance must have been related to the pressure resistance component. Generally, total resistance coefficients obtained from numerical simulations on the medium grid compare favorably with model test measurements. Thus, these coefficients were thought to be suitable to reliably predict resistance in head waves although resistance in the shortest wave at the highest frequency investigated ( $\tilde{\omega} \approx 2.15$ ) deviates significantly from measurements. However, this deviation was probably caused by insufficiently fine resolution of hull-induced waves on the medium grid.

Frictional resistance was related to the wetted hull surface considered. Simulations, performed also at  $F_n = 0.23$ , indicate that the wave-induced mean wetted hull surface was almost independent of wavelength and only slightly greater than the calm water wetted surface. The largest difference occurs in waves of frequency  $\tilde{\omega}$  of about 1.2, where the wave-induced mean wetted surface exceeded the calm water wetted surface by 1.6% at  $F_n = 0.16$  and by 0.5% at  $F_n = 0.23$ . This marginally growing wetted surface may have increased frictional resistance; however, wave grouping also led to higher total mean relative wave particle velocities compared with calm water conditions.

Figure 16 shows the diffraction and radiation components of total resistance obtained from numerical simulations. To determine the diffraction part, simulations were conducted in waves with the cruise ship totally restrained at its dynamic sinkage and trim position obtained from simulations in calm water. To compute the radiation part, simulations were performed in calm water with the ship executing prescribed heave and pitch motions obtained from simulations in waves. As expected, radiation, being about twice as large as diffraction, is the predominant part of total resistance in waves of  $\lambda/L$  ratios from about 0.8 to 1.1. Short waves did not generate radiation forces, and in long waves radiation and diffraction forces are nearly equal. Summing of radiation and diffraction force components did not yield the total resistance, especially in longer waves. Obviously the physical interaction between radiation and diffraction caused a reduction of total resistance.

Additionally, resistance in head waves for the ship

advancing at  $F_n = 0.16$  was simulated using codes COMET as well as OpenFOAM [12]. Numerical simulations were performed on the medium grid. Generally, results using code COMET agree more favorably with experimental measurements than results using code OpenFOAM. Only in waves of frequencies  $\tilde{\omega}$  in the neighborhood of unity, results using code OpenFOAM are closer to experimental measurements. Frictional resistance turned out to be about equally as small as that for the ship advancing at  $F_n = 0.23$ .

## Discussion and Conclusions

Predicting wave-induced resistance of ships in waves remains challenging. Nevertheless, its practical relevance motivated systematic investigations in the use of modern numerical methods to predict added resistance of ships in waves. For the two ship models investigated, RANS based field methods reliably predicted added resistance in head waves. However, they required an extensive computational effort, and associated anomalies like numerical diffusion in short waves had to be accounted for.

All experimental measurements available for comparison with numerical results were obtained from model tests. Therefore, to avert scaling errors, all numerical investigations were conducted at model scale.

The two RANS solvers OpenFOAM and COMET were used for the DTC and the cruise ship. Both methods were extended by an implicit solver to compute nonlinear six degrees-of-freedom ship motions. Generally, both codes yielded comparable results and agreed fairly well with model test measurements.

Systematic grid studies were performed. For simulations in calm water, grids comprising about  $1 \times 10^6$  cells (for one-half of the fluid domain) were sufficient to obtain reliable results. Coarse grids were suitable to predict ship motions. However, on the coarse grids, resistance in short waves was underestimated because discretization errors increased and, furthermore, the pressure part of resistance was small, whereas the frictional part of resistance remained nearly constant. In waves, the mean wetted surface remained almost constant and was only marginally higher than in calm water over the entire frequency range.

For the cruise ship, diffraction and radiation forces at different frequencies were investigated, whereby diffraction forces were obtained by restraining the

ship in waves, and the radiation forces, by prescribing the motions of the ship in calm water. In long waves, the sum of diffraction and radiation forces exceeded total resistance, i.e., the interaction of these two force components, which caused the reduction of total resistance, had to be accounted for. In short waves, the diffraction part of total resistance was dominant as almost no ship motions were induced.

## Nomenclature

$A$  = scalar volume fraction

$\mathbf{b}$  = body force

$B$  = ship breadth

$C_F$  = frictional resistance coefficient

$C_p$  = pressure resistance coefficient

$C_T$  = total resistance coefficient

$d$  = draft

$F_n$  = Froude number

$g$  = acceleration of gravity

$H$  = wave height

$I$  = unit tensor

$k$  = ship form factor

$L$  = ship length between perpendiculars

$m$  = mass

$\mathbf{n}$  = unit normal vector

$p$  = pressure

$r$  = refinement factor

$R_{aw}$  = average of added resistance in waves

$R_{calm}$  = calm water resistance

$R_F$  = frictional resistance

$R_T$  = total resistance

$R_W$  = wave-induced part of total resistance

$S$  = fluid surface

$S_F$  = wetted hull surface

$S_\zeta$  = spectral density of seaway

$t$  = time

$T$  = stress tensor

$T_m$  = draft amidships

$V$  = control volume

$\mathbf{v}$  = fluid velocity

$\nu_w$  = kinematic viscosity

$u_s$  = fluid surface velocity, ship speed

$y^+$  = cell thickness

$z_a$  = heave amplitude

$\theta_a$  = pitch amplitude

$\rho$  = density

$\rho_{\text{air}}$  = density of air

$\rho_{\text{eff}}$  = effective fluid density

$\rho_{\text{water}}$  = density of water

$\zeta_a$  = wave amplitude

$\mu$  = dynamic viscosity

$\omega$  = wave circular frequency

$\omega_e$  = encounter frequency

$\tilde{\omega}$  = nondimensional wave frequency

$\Delta$  = displaced volume

$\lambda$  = wavelength

$\nabla$  = Nabla operator



## References

1. Maruo, H., 1957, "The Excess Resistance of a Ship in a Rough Sea," *Int. Shipbuild. Prog.*, 4, pp. 337–345.

[Google Scholar](#)   [Crossref](#)

2. Boese, P., 1970, "A Simple Method for the Calculation of Resistance Increase of a Ship in a Seaway," *J. Ship Technol. Res.*, 17(86).

3. Gerritsma, J., and Beukelman, W., 1972, "Analysis of the Resistance Increase in Waves of a Fast Cargo Ship," *Int. Shipbuild. Prog.*, 19(217), pp. 285–293.

[Google Scholar](#)   [Crossref](#)

4. Ström-Tejsen, J., Hugh, Y. H., Yeh, and Moran, D. D., 1973, "Added Resistance in Waves," *SNAME Trans.*, 81, pp. 109–143.

5. Salvesen, N., Tuck, O. E., and Faltinsen, O. M., 1970, "Ship Motions and Sea Loads," *Society of Naval Architects and Marine Engineers Trans.*, 78, pp. 250–287.

6. Faltinsen, O. M., Minsaas, K. J., Liapis, N., and Skjoldal, S. O., 1980, "Prediction of Resistance and Propulsion of a Ship in a Seaway," 13th Symp. on Naval Hydrodynamics, Tokyo, pp. 505–529.

7. Liu, S., Papanikolaou, A., and Zaraphonites, G., 2011, "Prediction of Added Resistance of Ships in Waves," *J. Ocean Eng.*, 38(4), pp. 641–650.

[Google Scholar](#)   [Crossref](#)

8. Söding, H., Shigunov, V., Schellin, T. E., and El Moctar, O., 2014, "A Rankine Panel Method for Added Resistance of Ships in Waves," *ASME J. Offshore Mech. Arct. Eng.*, 136(3), p. 031601.

[Google Scholar](#)   [Crossref](#)

9. Kashiwagi, M., Ikeda, T., and Sasakawa, T., 2010, "Effects of Forward Speed of a Ship on Added Resistance in Waves," *J. Offshore Polar Eng.*, 20(3), pp. 196–203.

10. El Moctar, O., Oberhagemann, J., and Schellin, T. E., 2011, "Free Surface RANS Method for Hull Girder Springing and Whipping," *Society of Naval Architects and Marine Engineers Trans.*, 119, pp. 48–66.

11. Schellin, T. E., and el Moctar, O., 2007, "Numerical Prediction of Impact-Related Wave Loads on Ships," *ASME J. Offshore Mech. Arct. Eng.*, 129(1), p. 021602.

- 12Ley, J., Sigmund, S., and el Moctar, O., 2014, "Numerical Prediction of the Added Resistance of Ships in Waves," *33rd International Conference on Ocean, Offshore, and Arctic Engineering*, San Francisco, CA, OMAE Paper No. 2014-24216.
- 13Bertram, V., and Couser, P., 2014, "Computational Methods for Seakeeping and Added Resistance in Waves," 13th International Conference on Computer and IT Applications in the Maritime Industries COMPIT'14, Redworth, UK, pp. 8–16.
14. CD Adapco, 2011, "STAR-CCM+: User Guide 6.02.007," CD ADAPCO, New York.
15. OpenFOAM Foundation Ltd., 2011-2014, "OpenFOAM: User Guide," OpenFOAM Foundation, London.
16. Ferziger, J. H., and Peric, M., 2002, "Computational Methods for Fluid Dynamics," 3rd, ed., Springer Verlag, Berlin.

## Journal of Offshore Mechanics and Arctic Engineering

<a href="#">Issues</a>	<a href="#">Twitter</a>
<a href="#">Accepted Manuscripts</a>	<a href="#">About the Journal</a>
<a href="#">All Years</a>	<a href="#">Editorial Board</a>
<a href="#">Purchase</a>	<a href="#">Information for Authors</a>
<a href="#">Call for Papers</a>	
<a href="#">Rights and Permission</a>	

Online ISSN 1528-896X    Print ISSN 0892-7219

### Journals

[About ASME Journals](#)  
[Information for Authors](#)  
[Submit a Paper](#)  
[Call for Papers](#)  
[Title History](#)

### Conference Proceedings

[About ASME Conference](#)  
[Publications and Proceedings](#)  
[Conference Proceedings](#)  
[Author Guidelines](#)

### eBooks

About ASME eBooks  
ASME Press Advisory &  
Oversight Committee  
Book Proposal Guidelines

## Resources

Contact Us  
Library Service Center  
Frequently Asked Questions  
Publication Permissions &  
Reprints  
ASME Membership

## Opportunities

Faculty Positions



**STM** Member 2021

[Accessibility](#) [Privacy Statement](#) [Terms of Use](#)

[Get Adobe Acrobat Reader](#)

Copy This site uses cookies. By continuing to use our website, you are agreeing to [our privacy policy](#). [Accept](#)